Talanta 305 (2026) 129607

Contents lists available at ScienceDirect

Talanta

journal homepage: www.elsevier.com/locate/talanta

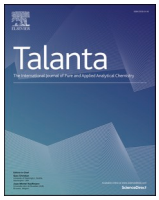

Bowtie-patterned MIM SERS platform assisted by machine learning for detection of pesticide residues in food matrices

Nazlı Öncer [a,1], Sümeyra Vural Kaymaz [a,b,1], Elmas Eva Öktem Olgun [c], Oltan Canli [c], Barış Güzel [c], Süleyman Çelik [a], Selim Tanrıseven [a], Hasan Kurt [d,e,f,*], Meral Yüce [a,**]

[a] SUNUM Nanotechnology Research and Application Centre, Sabanci University, Istanbul, 34956, Türkiye
[b] Department of Molecular Biology, Genetics, and Bioengineering, Faculty of Engineering and Natural Sciences, Sabanci University, Istanbul, 34956, Türkiye
[c] Climate Studies and Water Management Research Group, Climate and Life Sciences Vice Presidency, TUBITAK Marmara Research Center, 41470, Kocaeli, Türkiye
[d] Department of Bioengineering, Imperial College London, South Kensington Campus, London, SW7 2AZ, UK
[e] Department of Biomedical Engineering, School of Engineering and Natural Sciences, Istanbul Medipol University, Istanbul, 34810, Türkiye
[f] Research Institute for Health Sciences and Technologies (SABITA), Istanbul Medipol University, Istanbul, 34810, Türkiye

ARTICLE INFO

Keywords:
Pyrimethanil
Imidacloprid
Chlormequat chloride
Bowtie nanoarray
Unsupervised machine learning
Surface-enhanced Raman spectroscopy (SERS)

ABSTRACT

The increasing use of pesticides and their mixtures poses a serious risk to human health and the environment. This increases the demand for simple, cost-effective, and reliable methods for detecting these residues. In this study, a highly sensitive in-house SERS platform based on a metal–insulator–metal (MIM) nanoarray structure was employed to acquire Raman fingerprint spectra of Pyrimethanil (PYM), Imidacloprid (IMI), and Chlormequat chloride (CCC) in pepper juice, yielding spectra with high signal-to-noise ratios. The detection limit for PYM in pepper juice (0.16 mg/kg) was well below both the EFSA (2 mg/kg) and EPA (2 mg/kg) limits. Among the tested pesticides, PYM shows the lowest detection limit, indicating a more efficient signal enhancement for the π-metal interaction. This strong affinity results in significantly enhanced Raman scattering activity. Furthermore, the unsupervised machine learning analysis techniques (e.g., PCA and HCA) used showed a concentration-dependent separation in spiked samples. The same approach also enabled detection and discrimination in real food samples obtained from different regions. These results demonstrate the potential of the developed platform for rapid, on-site monitoring of pesticide residues in complex food matrices.

1. Introduction

The use of pesticide mixtures to protect plants from pests and diseases has become increasingly prevalent in agricultural production; these chemicals are generally applied by spraying on the surface of fruits and vegetables. Pyrimethanil (PYM) [N-(4,6-dimethylpyrimidin-2-yl)-phenylamine] is a fungicide belonging to the anilinopyrimidine group. It inhibits the activity of hydrolytic enzymes secreted by fungi during the infection, thereby preventing pathogen penetration into plant tissues and suppressing disease progression [1]. However, excessive or repeated application may lead to its accumulation in agricultural products, posing significant risks to human health and the environment [2]. Imidacloprid (IMI) is a high-solubility neonicotinoid insecticide with the chemical formula 1-[(6-chloro-3-pyridyl)methyl]-N-nitroimidazolidin-2-amine, exhibiting high persistence in soil and surface waters [3]. It targets nicotinic acetylcholine receptors in the nervous system of insects, causing persistent stimulation and paralysis [4]. Chlormequat chloride (CCC), chemically known as 2-chloroethyltrimethylammonium chloride, is a plant growth regulator (PGR) [5]. It is suggested that the inadvertent or uncontrolled use of these mixtures can harm fertility and even the developing fetus. Chronic exposure can lead to serious health problems, including convulsions, uncontrolled movements, asthma, congenital anomalies, paralysis, and ultimately death, due to the accumulation of acetylcholine in synapses [6,7].

To mitigate these risks and prevent the transfer of pesticide residues into the food chain, regulatory authorities such as the European Food Safety Authority (EFSA) and the US Environmental Protection Agency (EPA) have set strict maximum residue limits (MRLs) for individual

* Corresponding author. Department of Bioengineering, Imperial College London, South Kensington Campus, London, SW7 2AZ, UK.
** Corresponding author.
E-mail addresses: hasankurt@medipol.edu.tr (H. Kurt), meralyuce@sabanciuniv.edu (M. Yüce).
[1] These authors contributed equally to this work.

https://doi.org/10.1016/j.talanta.2026.129607
Received 11 November 2025; Received in revised form 16 February 2026; Accepted 28 February 2026
Available online 10 March 2026

pesticides. For example, EFSA has set MRLs of 2 mg/kg for PYM in pepper, 0.9 mg/kg for IMI, and 0.01 mg/kg for CCC. These regulations clearly underscore the urgent need for sensitive, rapid, and selective analytical methods to monitor pesticide residues in complex food matrices.

Currently, various methods are used to detect pesticide residues. These include high-performance liquid chromatography (HPLC) [8], gas chromatography (GC), gas chromatography-mass spectrometry (GC-MS) [9], liquid chromatography-mass spectrometry (LC-MS) [10], biosensor-based methods [11,12], and immunoassays [13]. Although these methods provide high accuracy and reproducibility, they suffer from several critical drawbacks, such as labor-intensive sample preparation, long analysis times, and the high cost and maintenance requirements of the instrumentation. In addition, their operation typically requires trained personnel, which further limits accessibility. Furthermore, GC methods generally cannot directly detect new polar neonicotinoid insecticides such as IMI because they are not highly volatile and are unstable when heated. Instead, these compounds are typically analyzed using HPLC or HPLC-MS systems [14]. However, these systems remain relatively expensive and typically require well-controlled laboratory conditions, which limit their applicability for on-site and field-based analyses.

In this context, Raman spectroscopy offers a distinctive advantage by providing molecule-specific structural information through well-defined vibrational fingerprints, enabling reliable identification of target analytes. Nevertheless, the practical application of Raman spectroscopy is often limited by its extremely small scattering cross section (~10^{-30} cm^2 $molecule^{-1}$), resulting in inherently weak signal intensities. [15]. This makes it particularly challenging to detect very low levels of pesticide residues and complicates the spectral differentiation of pesticides with similar structures in food matrices. To overcome these limitations, SERS has been developed, which amplifies Raman signals by exploiting plasmonic “hot spots” generated at the interface between analyte molecules and metallic nanostructures [16–18]. In particular, the metal–insulator–metal (MIM) architecture concentrates electromagnetic fields between metallic layers, creating "hot spot" regions on the surface; this results in improved signal-to-noise ratios and increased detection sensitivity [19].

This study proposes machine-learning-based SERS detection of PYM, IMI, and CCC using an in-house 785 nm Raman instrument equipped with a MIM-based SERS bowtie nanoarray. The proposed SERS platform enables rapid, label-free, and highly sensitive detection of pesticide residues, exhibiting excellent signal stability, reproducibility, and strong Raman enhancement. In addition, the machine learning analyses employed provided clear concentration-dependent discrimination of spiked samples and robust spectral separation of samples collected from different regions. This platform also offers strong applicability and field potential for monitoring pesticides in real samples under real environmental conditions. Scheme 1 describes the MIM-based SERS bowtie platform and machine learning-assisted SERS application for the detection of pesticides in pepper juice.

2. Experimental section

2.1. Materials and instrumentation

Pyrimethanil (2-Anilino-4,6-dimethylpyrimidine) (53112-28-0), Imidacloprid (138261-41-3), Chlormequat chloride ((2-Chloroethyl) trimethylammonium chloride) (999-81-5), Metalaxyl (*N*-(2,6-Dimethylphenyl)-*N*-(methoxyacetyl)-DL-alanine methyl ester) (57837-19-1), Ametoctradin (5-Ethyl-6-octyl [1,2,4]triazolo[1,5-*a*]pyrimidin-7--amine) (865318-97-4) pesticides were purchased from Sigma-Aldrich (St. Louis, MO, USA). At the same time, silicon wafers were obtained from MicroChemicals GmbH (Ulm, Germany).

Raman measurements were obtained using an in-house Raman spectrometer, which we explained in detail in our previous publication [20]. In summary, the high-resolution Raman spectrometer used in the study was designed with a narrow-linewidth diode laser at 785 nm and a maximum power of 400 mW. The laser beam is transmitted through a fiber connection and focused onto the sample via a light-splitting prism, mirrors, filters, and a dichroic mirror. The excitation and scattered signals are collected using high-magnification objectives and directed to the spectrometer-CCD detector combination. Additionally, a CMOS camera is integrated for monitoring and imaging the system. Sample positioning is achieved using joystick-controlled motion systems, and data collection and processing are carried out using Solis software. Measurements were performed at a laser power of 100 mW, 40X magnification, 30 acquisitions with a 2-s exposure time in the 400–1800 cm^{-1} range.

2.2. The fabrication of bowtie metasurface as a SERS platform

The silicon wafers underwent pre-cleaning with piranha solution and oxygen plasma and were carefully dried before deposition. A 10 nm Ti adhesion layer and a 100 nm thick layer of Al were deposited using the process of thermal evaporation. A 75 nm thick SiO_2 insulating layer was grown, followed by the process of plasma-enhanced chemical vapor deposition (PECVD). CSAR 6200.09 positive photoresist was coated at a speed of 6000 rpm, giving a photoresist thickness of about 340 nm. After soft baking at 150 °C for 120 s, the nanostructures were patterned by electron beam lithography (EBL) at a surface charge density of 280-290 μC cm^{-2}. The deposition of 10 nm of Ti and 100 nm of Au was thermally evaporated, followed by a lift-off process by CSAR remover (AR 600-71) to achieve MIM nanostructure bowties. The structural properties of the synthesized substrates were investigated using a scanning electron microscope (SEM, Zeiss Leo Supra VP 3). In addition, the chemical composition was verified by energy-dispersive X-ray analysis (EDS). Optical characterization of the MIM bowtie metasurface was performed by reflectance measurements to evaluate its resonance behavior. The SERS performance of the substrates was assessed using Rhodamine 6G (R6G) as a standard probe molecule. Based on the comparative Raman intensities obtained from the MIM bowtie substrates and a reference planar Si wafer substrate, the SERS enhancement factor (EF) was

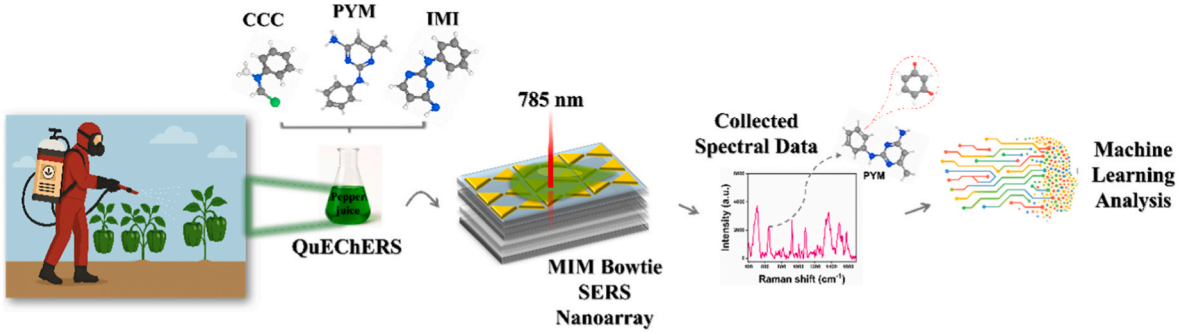

Scheme 1. Illustration of the MIM-based bowtie SERS platform and machine learning-assisted SERS analysis for detecting pesticide residues in pepper juice.

calculated [21].

2.3. Sample collection and preparation

Pepper samples were obtained from four distinct regions in Türkiye: M2 (naturally grown in gardens, Sakarya), M3 (Antalya), M4 (Elmalı), and M7 (Mersin). Sample preparation was performed using the Quick Easy Cheap Effective Rugged Safe (QuEChERS) extraction protocol with minor modifications, following a previously reported method [21]. The samples were ground using a blender and weighed out at 5 g each into Falcon tubes. 5 mL of acetonitrile and a QuEChERS salt mixture (containing MgSO4, NaCl, and trisodium citrate) were added, and the mixture was mixed for 2-3 min until the tube warmed up. After ensuring the mixture was homogeneous, it was centrifuged at 3000 rpm for 5 min. The supernatant phase was carefully collected, filtered through a 0.45 μm membrane filter, and transferred to glass vials, which were stored at −20 °C until further analysis.

Stock solutions of PYM, IMI, CCC, and Ametoctradin (AME) were prepared in methanol, whereas Metalaxyl (MTX) was dissolved in acetonitrile at a concentration of 10^{-2} M. The stock solutions were subsequently diluted with deionized water to obtain working standards. A clean pepper juice matrix (M3: Antalya), previously confirmed to be free of target analytes via LC-MS analysis (Table S3), was used as the blank matrix for spiked sample preparations. Final concentrations were adjusted to 10^{-9} M to 10^{-4} M for SERS calibration. Additionally, a spiked sample was created for the simulated contaminated sample by adding the amount of pesticide detected in the M3 sample by LC-MS results (10^{-6} M for IMI and 10^{-8} M for PYM).

2.4. The collection and processing of SERS spectral data

Measurements were obtained using an in-house 785 nm Raman instrument (1800-400 cm^{-1}) as used in our previous study. Spectra were obtained using a 40 × objective and a 9 μW laser power, with 30 accumulations and an integration time of 2 s; at least 15 spectra were collected from each sample. Raman spectral data were preprocessed using a Python-based pipeline (RPlot) developed on the RamanSPy framework [22]. The pipeline provides multiple preprocessing options, including a range of baseline correction and denoising algorithms. In this study, spectral noise was reduced using the Savitsky–Golay smoothing filter, while baseline contributions were corrected using the IARPLS and ARPLS algorithms. Peak position identification and labeling were performed using the pipeline's built-in peak-picking functions. Importantly, all preprocessing steps were applied uniformly to the entire dataset using identical parameters, and the processed spectra were exported as a single data file.

Spectral data were normalized using a min–max normalization procedure to ensure intensity scale compatibility across datasets. The normalization was performed according to the equation ($Y_{norm} = Y\text{-}Y_{min}/Y_0\text{-}Y_{min}$) where Y is the measured spectral intensity, Y_{min} is the minimum intensity within the selected spectral range, and Y_0 corresponds to the intensity of the reference background peaks located at 925, 1003, 1082, and 1266 cm^{-1}. Limits of detection (LoD) were determined from calibration curves fitted using logistic regression. The LoD was calculated using the formula of $C1 + 3.3 \times C2$, where C_1 represents the mean normalized intensity of the blank sample at the selected spectral position, and C_2 denotes the standard deviation of the normalized intensity measured at the same location. As summarized in Table S17 (Supporting Information), substrate-to-substrate LoD evaluation based on the 3σ criterion revealed analyte-dependent sensitivity, with matrix-equivalent detection limits of 66.2 ppm (IMI), 0.15 ppm (PYM), and 15.3 ppm (CCC).

2.5. Multivariate data analysis

2.5.1. Unsupervised analysis

Unsupervised multivariate analyses were performed using the spectroscopy application of Origin 2024 software. Principal Component Analysis (PCA) and Hierarchical Clustering Analysis (HCA) were applied to the entire spectral dataset without using class labels to explore the intrinsic data structure and spectral variability. PCA results were visualized as two-dimensional score plots, while HCA results were presented as circular dendrograms. These analyses were used to assess clustering tendencies and natural separation among samples based solely on spectral features.

2.5.2. Supervised analysis

Supervised multivariate analyses were conducted using Unscrambler X 10.4 software to evaluate classification performance and the reliability of the Bowtie SERS platform. Labeled datasets were randomly divided into training and test sets for each sample group. Within the supervised modeling pipeline, PCA was first applied to the training datasets as a dimensionality reduction step, and the resulting principal components were subsequently used as input variables for classification. Linear Discriminant Analysis (LDA), Support Vector Machine (SVM), and Soft Independent Modeling of Class Analogy (SIMCA) were employed for supervised classification. Model performance was evaluated using classification accuracy metrics, and the results of LDA and SVM were visualized through score and distribution plots. For SIMCA, class separation and inter-sample distances were assessed using column and Coomans plots. Classification outcomes were summarized using confusion matrices and corresponding statistical tables [20,23].

3. Results and discussion

3.1. Bowtie metasurfaces: fabrication and SERS performance

The multilayer architecture of the substrate is schematically presented in Fig. 1a. It is composed of a silicon wafer base, followed by a Ti adhesion layer, an Al reflective layer, a SiO_2 dielectric spacer, and an Au plasmonic layer deposited on the surface. This metal–insulator–metal configuration has been widely reported to support strong confinement of plasmonic modes within the dielectric gap, thereby promoting intense electromagnetic field localization and enhanced light–matter interaction [19,24]. Furthermore, the integration of the Al reflective layer optimizes resonance conditions, while the top Au layer creates chemically stable plasmonic hotspots, thus amplifying the SERS signal. FIB-SEM (Focused Ion Beam), TEM-EDX (Transmission Electron Microscope–Energy Dispersive X-ray Analysis) analyses, and SEM images pertaining to the MIM structure are shown in Fig. 1b. The image obtained with FIB-SEM enables high-resolution observation of the layered architecture of the structure, while TEM-EDX analysis determines the positions of each element in the MIM structure and the boundaries between the layers. EDX maps for each element show that the coatings are uniform and have reached the desired thickness (Fig. 1c). The SEM image reveals the homogeneous morphology of the Au bowtie structures and their regularity on the substrate. This regularity plays a critical role in minimizing signal fluctuations arising from morphological heterogeneity. The presence of hot spot regions evenly distributed across the surface indicates that the Raman signal is not confined to localized areas but is spread across the entire active sensing surface (Fig. 1d).

After evaluating the morphological properties of the MIM-based bowtie SERS nanoarray, its optical properties were assessed. The platform exhibits two distinct LSPR modes, one close to 785 nm laser excitation (~788 nm) and the other coinciding with the Stokes scattering region (~900 nm), providing a broadband, dual-mode response (Fig. 1e). Consistent with this optical behavior, the MIM-BTA architecture demonstrates superior SERS performance compared to control substrates. Although the laser power and analyte concentrations are not

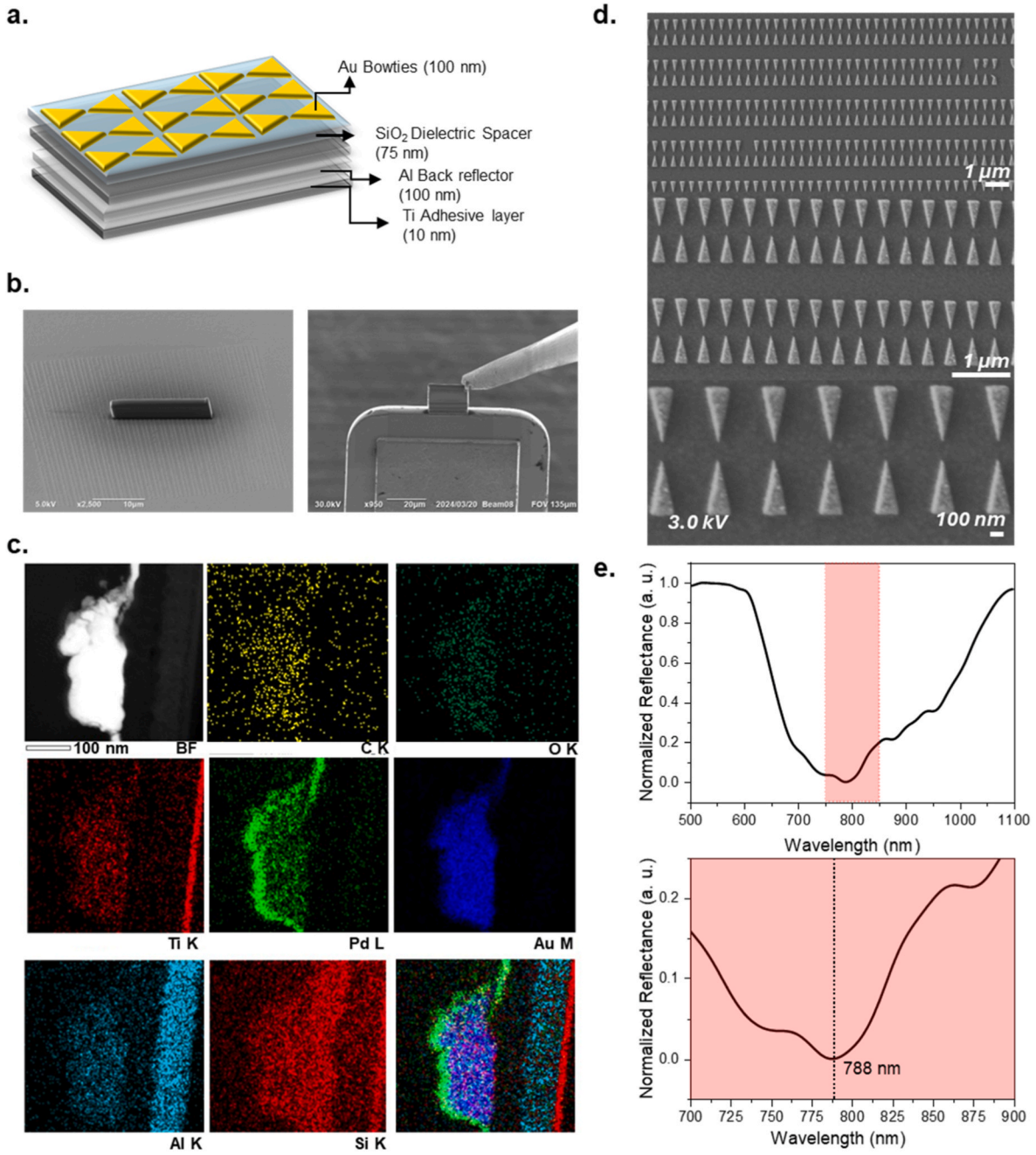

Fig. 1. Structural and optical characterization of the MIM-based bowtie SERS substrate. a. Schematic illustration of the multilayer architecture consisting of a Si substrate, Ti adhesion layer (10 nm), Al back reflector (100 nm), SiO_2 dielectric spacer (75 nm), and patterned Au bowtie nanoarray (100 nm) **b.** SEM images showing large-area patterned nanoarrays with uniform periodic geometry. **c.** Cross-sectional FIB–SEM and TEM–EDS analyses confirming multilayer thicknesses and interfaces. Corresponding elemental maps (C, O, Al, Si, Ti, Au, Pd) reveal the spatial distribution of constituent elements across the structure. **d.** High-magnification SEM image of the nanoarray demonstrating the uniform bowtie morphology and nanoscale feature definition. **e.** Measured optical reflection spectrum of the metasurface showing a resonance minimum centered at ~788 nm.

identical across all substrates, these experimental parameters are explicitly reported in the corresponding figures and captions to ensure full transparency. Importantly, such differences do not obscure the observed performance trends; instead, they further highlight the robustness of the MIM-BTA design under more stringent measurement conditions. Specifically, for MTX, characteristic Raman features are clearly resolved on the MIM-BTA substrate at lower analyte concentrations, whereas comparable signals are absent or significantly weaker on control substrates measured at higher concentrations. Similarly, for Rhodamine, the Au-BTA substrate required 200 mW of laser power to generate detectable Raman signals, whereas the MIM-BTA substrate achieved comparable signal intensities at only 20 mW, indicating a markedly higher electromagnetic enhancement efficiency (Fig. S5) [21].

As summarized in Table S18 and S19 and supported by SEM images in Fig. S8, the platform exhibits fabrication reproducibility across three independent batches, with an inter-batch Raman signal RSD of 7.88% (645 cm^{-1} PYM band). Although nanoscale gap variations (RSD 13.81%) were observed, the lower signal variability confirms that analytical performance is predominantly governed by the collective plasmonic response rather than minor geometric differences.

3.2. SERS detection of PYM, IMI, and CCC on MIM-based bowtie nanoarrays and evaluation of substrate performance

Figs. 2 and 3 show the results obtained for the determination of PYM, IMI, and CCC using an in-house Raman spectroscopy system, along with analyses of the substrate's detection performance. The concentration-dependent SERS measurements of these pesticides in aqueous solution and pepper juice are analyzed.

Representative spectra of PYM, IMI, and CCC recorded at different concentrations (Fig. 2a–c) exhibit well-resolved characteristic vibrational bands that remain distinguishable even at low analyte levels, confirming the strong enhancement capability and spectral selectivity of the platform. The progressive decrease in peak intensity with decreasing concentration demonstrates a clear concentration–response relationship

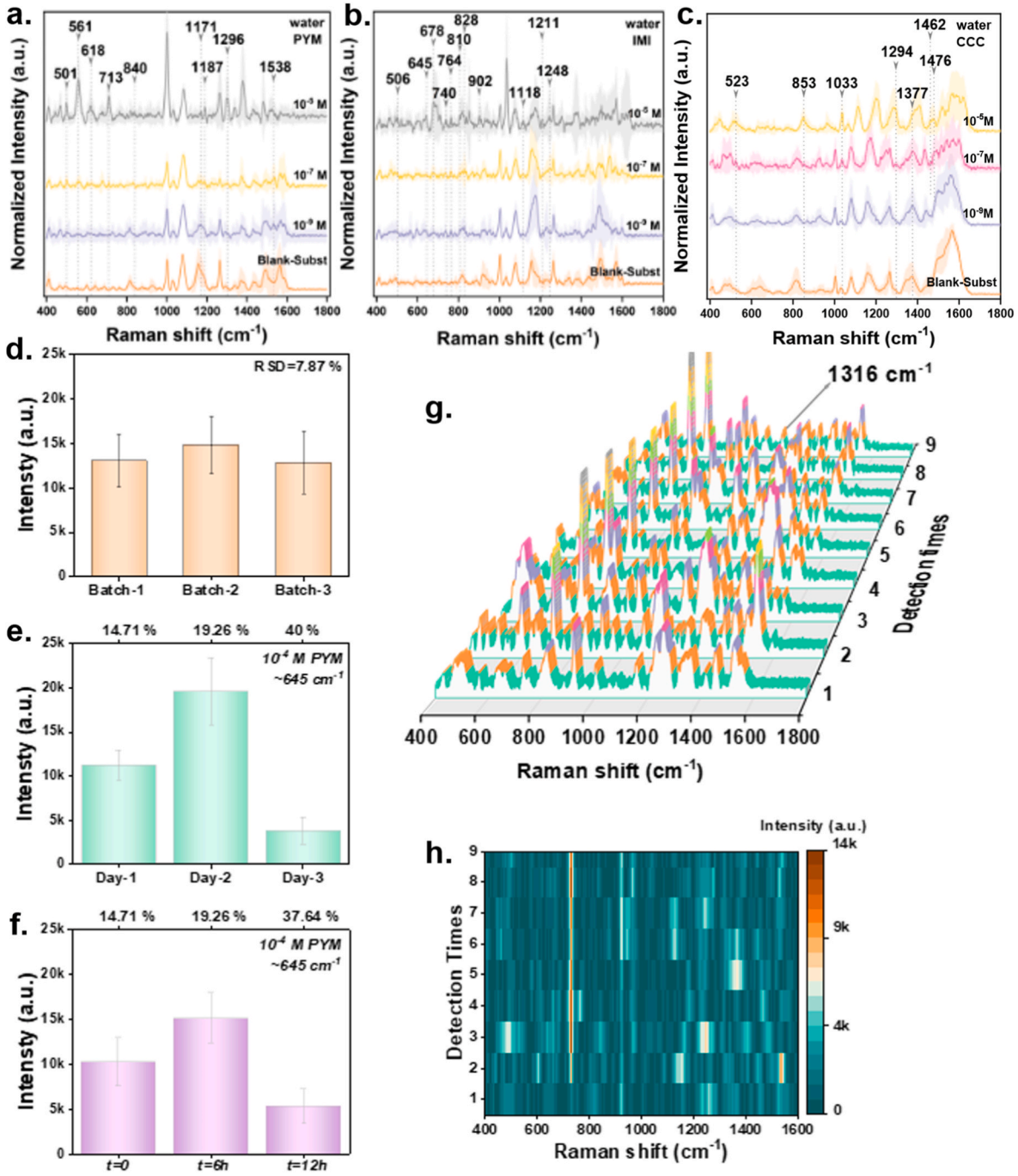

Fig. 2. Comprehensive evaluation of analytical performance, reproducibility, and stability of the SERS metasurface platform. a–c. Representative SERS spectra recorded for three analytes (PYM, IMI, and CCC) at different concentrations, together with blank substrate and water controls. Characteristic Raman bands used for identification are labeled. Signal intensity decreases systematically with concentration, while diagnostic peaks remain distinguishable down to trace levels, demonstrating sensitivity and spectral specificity. **d.** Batch-to-batch reproducibility was assessed using three independently fabricated substrates. Comparable signal intensities with an overall RSD of 7.87% confirm fabrication consistency. e. Inter-day stability was evaluated over three days using the characteristic ~645 cm^{-1} band of PYM, showing moderate variation attributable to environmental or measurement fluctuations. **f.** Short-term temporal stability was measured at t = 0, 6 h, and 12 h, indicating gradual signal attenuation yet preserved spectral detectability. **g.** SERS spectra of CCC recorded in pepper juice. **h.** The thermal stability of CCC at 10^{-5} M in pepper juice under continuous laser irradiation is demonstrated using a MIM-based bowtie SERS nanoarray.

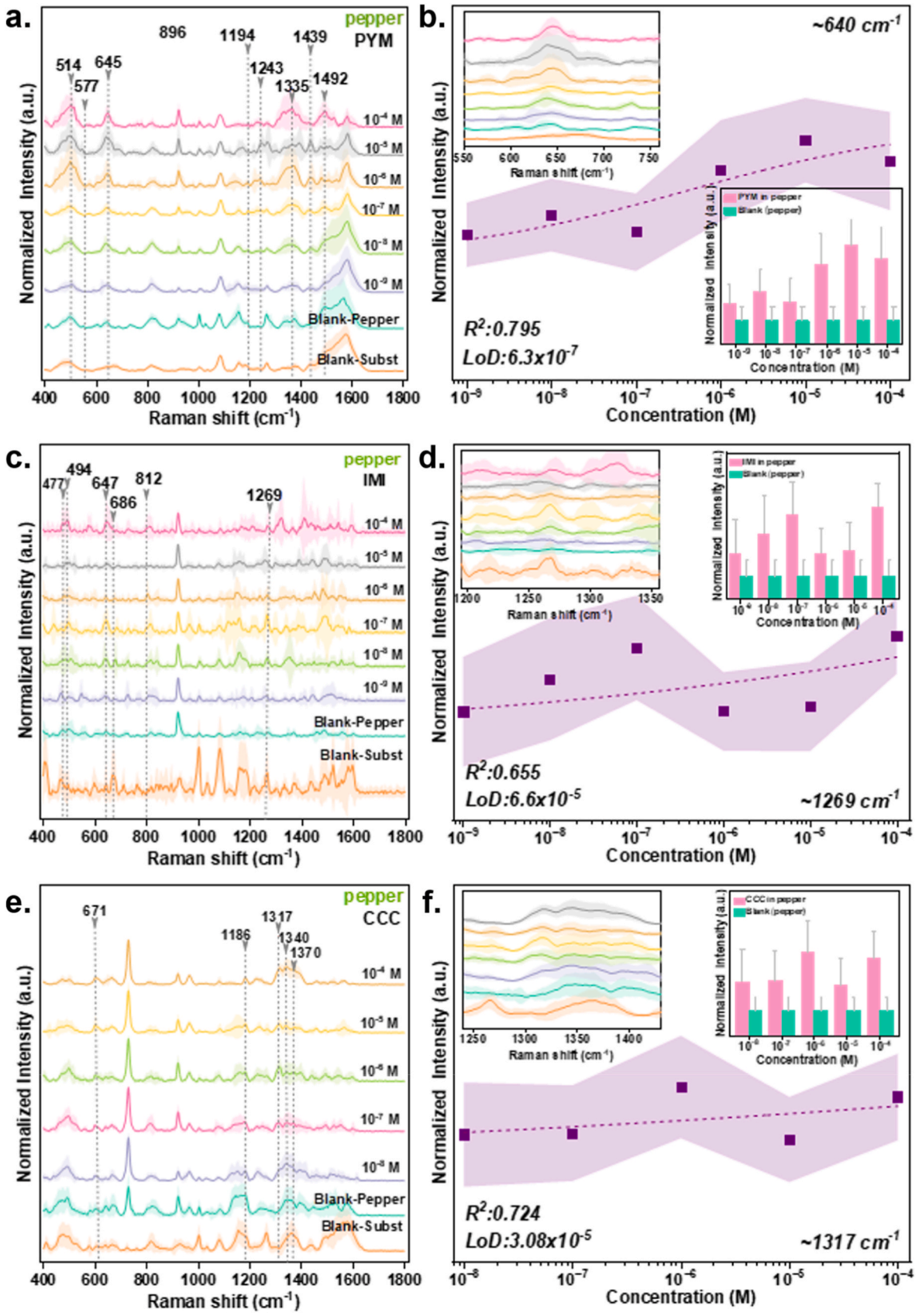

(caption on next page)

Fig. 3. SERS detection of PYM, IMI, and CCC in pepper matrix. a. SERS spectra of PYM at different concentrations measured in pepper extract. Characteristic Raman bands are labeled, and intensity variations with concentration are clearly visible. **b.** Calibration plot constructed from the characteristic ~640–645 cm^{-1} band of PYM in pepper, showing concentration-dependent signal increase. The inset displays stacked spectra highlighting spectral evolution, and the bar chart summarizes normalized intensity changes of the same band across concentrations. The calculated linearity and detection limit are also indicated. **c.** SERS spectra of IMI at different concentrations recorded in pepper extract. Distinct vibrational bands are preserved across the concentration range, demonstrating selective detection within the complex matrix. **d.** Calibration curve obtained using the characteristic ~1269 cm^{-1} band of IMI in pepper. The inset shows spectral zoom, while the bar chart presents intensity variation versus concentration for the selected band. **e.** SERS spectra of CCC measured at varying concentrations in pepper extract. Diagnostic Raman peaks remain identifiable even at low concentrations, confirming analytical sensitivity. f. Quantitative response plot based on the characteristic ~1317 cm^{-1} band of CCC in pepper. The inset stacked spectra and bar chart further illustrate concentration-dependent signal enhancement and reproducibility for the selected vibrational mode.

without noticeable peak shifts, indicating stable plasmonic resonance behavior and negligible spectral distortion. To assess fabrication reproducibility, measurements were performed on three independently prepared substrate batches (Fig. 2d). Comparable signal intensities were obtained, yielding an overall relative standard deviation (RSD) of 7.87%, which confirms high batch-to-batch consistency. In addition, spatial reproducibility was evaluated by collecting spectra from 15 randomly selected spots on each substrate under identical experimental conditions. Temporal stability was further investigated through both interday (Fig. 2e) and intraday (Fig. 2f) measurements using the characteristic ~645 cm^{-1} band of PYM as a probe signal. While moderate intensity variations were observed over time, diagnostic peaks remained clearly detectable, demonstrating that the substrate maintains analytical functionality despite signal fluctuations. Such behavior is typical of plasmonic systems, where minor environmental or adsorption differences can influence absolute intensity without altering spectral fingerprint integrity.

The detected peaks for PYM are shown as dotted lines, and the characteristic peaks at 501 cm^{-1} in water and 645 cm^{-1} in pepper juice increased with concentration (see Table S1 for the complete assignment table). It is thought that the difference between these peaks in water and pepper juice may be due to the nature of Raman scattering, where compounds such as carotenoids and pigments in pepper juice either mask or attenuate the 501 cm^{-1} peaks (a similar trend was observed for IMI and CCC). Therefore, LoD was calculated for the 645 cm^{-1} peaks, which showed a positive concentration-dependent trend in the pepper juice (Fig. 3b). The LoD of 6.3×10^{-7} mol/L was found to be well below the maximum residue limits (MRLs) set by the EPA, 2025noting that pepper was not specifically reported [23],EFSA, 2024 MRL of 2 mg/kg [25], and the Turkish Ministry of Agriculture and Forestry MRL of 2 mg/kg [26]. To support the LoD calculations, the concentration-dependent increase of the pesticide-specific Raman peak (645 cm^{-1}) in the pepper juice was also displayed as a column chart. This analysis clearly demonstrated selective detection of the pesticide even in complex food matrices, with a distinct increase in signal intensity as analyte concentration increased. Similarly, the concentration-dependent peaks detected in aqueous and pepper juice samples of IMI are shown in Fig. 3c and d, respectively. The characteristic peaks at 1269 cm^{-1} in pepper juice showed a partial but significant increase in concentration. The obtained LoD value of 6.6×10^{-5} mol L^{-1} was higher than the maximum residue limits established by EPA, 2025 (1 mg kg^{-1}), EFSA, 2024 (0.9 mg kg^{-1}), and the Turkish Ministry of Agriculture and Forestry (0.9 mg kg^{-1}). Nevertheless, the platform demonstrates strong analytical capability compared with previously reported methods, particularly in key performance metrics such as detection limit, analysis time, and machine learning–assisted evaluation (Table S2). Comparable analytical behavior was also observed for the CCC pesticide. The column plot shows the variation in the CCC signal intensity at 1317 cm^{-1} over the concentration range of 10^{-8}–10^{-4} M in pepper extract. Although the band intensity increases with concentration, the response deviates from ideal linearity. Such behavior is well known in SERS-based measurements and can arise from multiple factors. First, SERS enhancement is governed by spatially heterogeneous localized electromagnetic hotspots, meaning that signal intensity does not always scale linearly with analyte concentration, especially as active adsorption sites approach saturation at higher concentrations [27–29]. Second, matrix-related interactions, such as hydrogen bonding or intermolecular adsorption between CCC molecules and components of the pepper extract, may introduce additional variability in signal response [30]. Similar partially nonlinear trends have also been reported for PYM, CCC, and related systems in the literature [31,32]. Despite these effects, the clear concentration-dependent increase observed for the 1317 cm^{-1} band confirms that CCC can be selectively detected within a complex food matrix, demonstrating the practical applicability of the developed SERS platform.

The results obtained for CCC in both aqueous and pepper matrices are presented in Figs. 2c and 3e. In aqueous measurements, performed over the concentration range of 10^{-4}–10^{-8} mol L^{-1}, the most pronounced concentration-dependent intensity variation was observed at the 1033 cm^{-1} band, indicating that this mode is the most suitable analytical marker for quantitative evaluation in water. In contrast, for the pepper matrix, LoD calculations were based on the characteristic 1317 cm^{-1} band (Fig. 3f), which exhibited a clear positive trend with increasing concentration, yielding a detection limit of 3.08×10^{-5} mol L^{-1}. Notably, the sensitivity to PYM (fungicide) was distinctly higher than that to IMI (insecticide) and CCC (plant growth regulator). This difference is most likely related to molecular structure–surface interaction effects. Specifically, the 645 cm^{-1} band of PYM, assigned to C–H out-of-plane bending and ring deformation of the phenyl group (Fig. S1 for vibrational assignment), can promote stronger π–metal interactions with the Au nanostructures. Such interactions enhance adsorption efficiency and local electromagnetic coupling, ultimately leading to stronger SERS enhancement [30,33,34]. Taken together, these findings indicate that the developed MIM-based SERS platform provides selective and highly sensitive detection, with particularly strong performance for fungicide molecules that possess aromatic ring systems capable of efficient surface coupling.

Achieving a high-quality SERS response is directly dependent on the thermal stability and structural uniformity of the substrate [35,36]. CCC in pepper juice was used to evaluate the SERS performance of the MIM-based bowtie SERS nanoarray (Fig. 2g–h). The SERS sensor demonstrated thermal stability with 9 measurements taken from the same location and an RSD of 7.27%. A detailed map of the characteristic peak at 1317 cm^{-1} is also presented in Fig. S2. Machine Learning–Assisted Spectral Analysis of Pesticide Mixture Fig. 4a illustrates the machine learning-supported SERS application of the MIM-based SERS bowtie platform for detecting pesticides in pepper juice. PCA was performed in the 400-1800 cm^{-1} range (n = 61) to examine the concentration-dependent spectral separation of pesticides in pepper juice. PCA analysis revealed that the spectral data of the pesticide concentrations in pepper juice solutions at 10^{-9} M (9), 10^{-4} M (4), and blank (pepper juice) were clearly separated Fig. 4b). PCA explained approximately 92% of the total variance in the PC axes, indicating that the differences in the chemical fingerprints of these three groups were substantial. This situation suggests that the variation in pesticide concentration directly reflects in the SERS spectrum, with the differences in the intensity of characteristic Raman bands playing a predominant role in differentiation. HCA was performed to confirm the PCA results (Fig. 4c). In the HCA analysis, the samples were observed to be grouped into three distinct clusters (blank (pepper juice), 10^{-9} M:9, and 10^{-4}:4

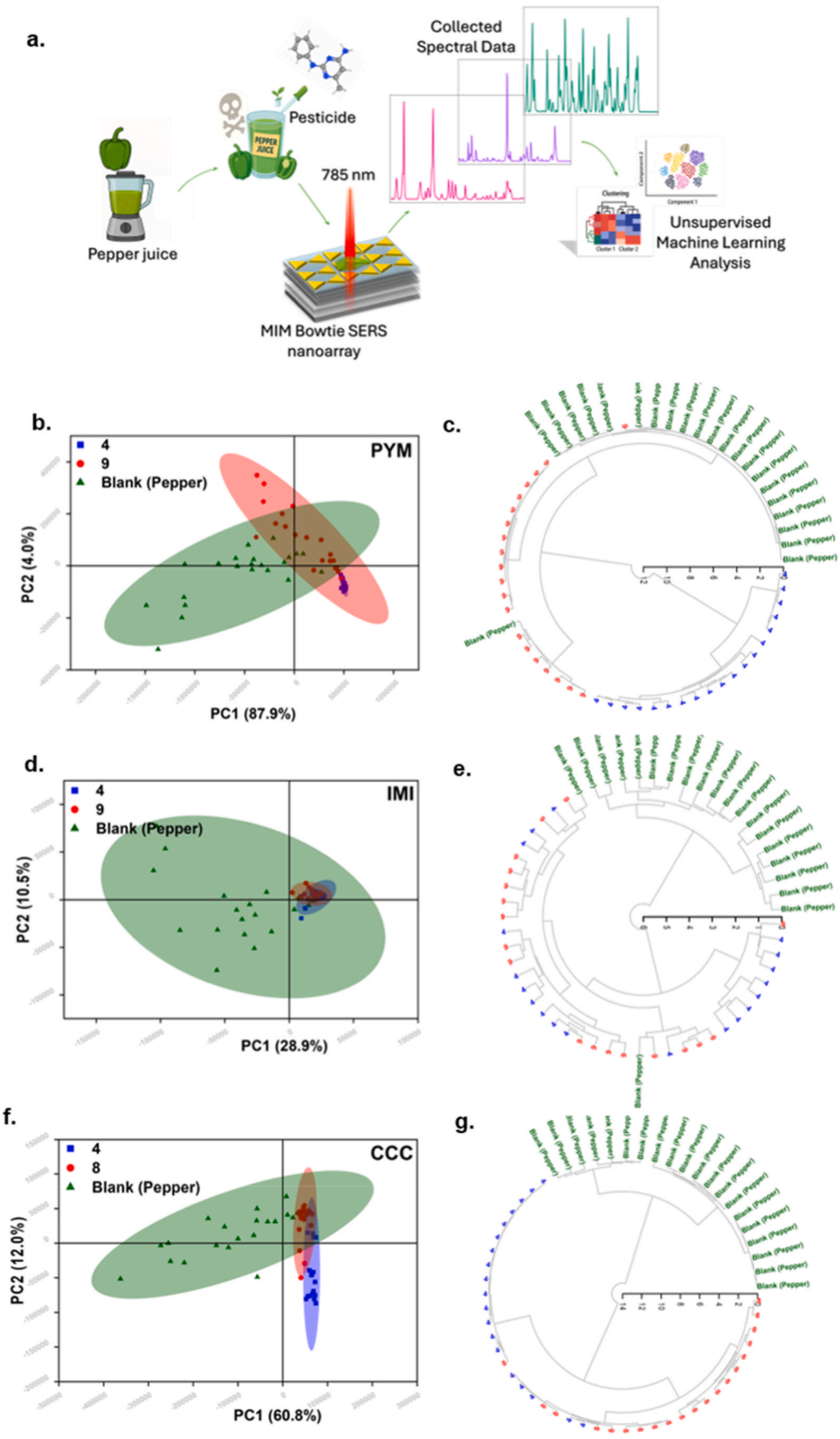

(caption on next page)

Fig. 4. Results of unsupervised machine learning analysis of SERS spectra of pepper waters treated with pesticides. **a.** Schematic representation of pesticide detection. **b.** PCA analysis of spectral data of PYM pesticide in pepper juice obtained from 4 (10^{-4} M), 9 (10^{-9} M), and blank (pepper juice) solutions. **c.** HCA visualized in a circular dendrogram obtained from the same data set using Ward's algorithm. **d.** PCA analysis of spectral data of IMI pesticide in pepper juice obtained from 4 (10^{-4} M), 9 (10^{-9} M), and blank (pepper juice) solutions. **e.** HCA visualized in a circular dendrogram obtained from the same data set using Ward's algorithm. **f.** PCA analysis of spectral data of CCC pesticide in pepper juice obtained from 4 (10^{-4} M), 8 (10^{-8} M), and blank (pepper juice) solutions. **g.** HCA visualized in a circular dendrogram obtained from the same data set using Ward's algorithm.

M), with distinct separation between clusters. The circular and isolated arrangement of the clusters in the dendrogram indicates weak spectral similarity between the groups and high intra-group homogeneity. Similar trends can be observed for the analysis conducted for IMI and CCC. PCA-HCA results for IMI indicate that the blank (pepper juice) group was completely separated from the 10^{-9} M (9) and 10^{-4} M (4) samples, but the two concentrations were heavily mixed (Fig. 4d–e). This is the primary reason for the relatively low separation percentage (39.4%). The overlap in signal intensities can be explained by the 10^{-9} M level remaining near the LoD (9.14x10-5 M) and by matrix components (sugar, phenolic, pigment) competing for surface adsorption. Thus, the SERS response obtained for IMI exhibited statistically significant but limited discrimination at lower concentrations. In the CCC analysis, the blank (pepper juice) set was again clearly separated, and the signal-to-noise ratios for the lower concentration levels of 10^{-8} M (8) and 10^{-4} M (4) (LoD level) were more stable, resulting in a statistically significant difference between the two groups (Fig. 4f–g). The total variance was 72.8%, indicating that the spectral response of CCC was more consistent and reproducible than that of IMI.

This trend observed for both pesticides is consistent with the substrate's higher chemical compatibility with PYM. The π-metal interaction between the aromatic ring in the PYM structure and the SERS-active surface enhanced both PCA variance (92%) and HCA discrimination acuity, enhancing the effectiveness of Raman scattering. Therefore, it can be concluded that the sensor's selectivity is strongly influenced not only by concentration and matrix factors but also by the analyte's chemical structure and surface affinity.

In this context, performing analyses across the entire spectral range (400-1800 cm^{-1}) is a critical factor for enhancing discrimination. While some studies in the literature use only selected Raman regions (e.g., 500-700 cm^{-1} and 950-1300 cm^{-1}) [1]. This study incorporates variations in regions of low intensity but high informative value into the model by evaluating the entire range. Thus, the sensor–analyte interactions are captured holistically rather than confined to specific bands, thereby improving the reliability and robustness of statistical discrimination.

Following the successful results obtained with PCA and HCA, linear and nonlinear supervised analysis methods were applied to determine and prove the classes of pepper juice and pesticides with different concentrations. In this context, training and test data sets were created using randomly selected data from the sample groups, and classification models were developed based on these data sets. The LDA analysis performed using the entire spectral dataset and a single PCA transformation is summarized in Fig. S3. According to the results, the classification accuracies were 83.64% for PYM, 62.75% for IMI, and 90.91% for CCC. These findings indicate that the vast majority of test samples could be correctly assigned to their respective classes. The achieved accuracy is also evident in the matrix tables showing the predicted and observed class distributions for the training datasets (see Table S4–S9). The second analysis, SIMCA, allows evaluation of the similarity and distance relationships of the samples to the created class models rather than a direct distinction between classes. In this context, separate SIMCA models were created for each pesticide group based on the PCA results, and the positions of the samples in these models are presented in Fig. S4. Fig. S4a shows the distances between the PCA models created for PYM. The distinct distance between the models indicates that pesticide groups with different concentrations are well separated from each other and that the class models are consistently created. Fig. S4b and S4c present the distances of the samples from the relevant class models using Coomans plots. The 5% significance threshold used in these plots indicates that the results are statistically reliable. The green dots represent randomly selected test samples for each group. Partial overlap in some test samples between class models is expected, especially for pesticide groups with similar concentrations. This situation can be attributed to the natural variation of SERS spectra measured in a complex matrix, such as pepper juice, and the fact that analyte signals at low concentrations exhibit similar spectral characteristics. Similarly, the results for IMI and CCC are presented in Fig. S4. Upon examination, the test samples exhibit partial overlap and interclass approximations, particularly near the class boundaries, similar to the situation observed for PYM. This situation may stem from spectral similarities among samples with similar concentrations and complex matrix effects.

Finally, SVM analysis was performed using PC loading spectra associated with the pesticide peaks as references. In this context, SVM classification graphs based on Raman bands specific to pesticides) located in the ranges of 1076–1567 cm^{-1} for PYM, 1160–1580 cm^{-1} for IMI, and 730–1571 cm^{-1} for CCC, are presented in Fig. 5. As a result of the analyses, 100% classification accuracy was achieved on the training data, and over 65% validation accuracy was achieved on the test data. These accuracy values are also supported by matrix tables showing the predicted and observed class distributions. Detailed results for the relevant test classes are presented in Table S10–15.

These supervised machine learning analyses demonstrated that SERS spectral data obtained from pesticide-treated and pesticide-free samples at different concentrations exhibited high classification performance. The results obtained confirm the reliability of the proposed approach and validate the Bowtie-based SERS platform developed as an effective and efficient analytical tool for pesticide detection.

3.3. *In-depth investigation of samples obtained from different regions*

Analyses were performed using a MIM-based bowtie SERS nanoarray for pepper samples obtained from different regions. The SERS spectra obtained from blank (substrate), M2, M4, and M7 pepper juices are shown in Fig. 6a. The M7 sample exhibited distinct spectral differences, clearly indicative of contamination. As shown, characteristic peaks were detected at 1366, 1458, 1479, 1518, and 1582 cm-1, which are present only in this sample. Band assignments were made for this evaluation by reference to the characteristic peak positions reported in our previous study [20]. In the clean samples (M2, M4), these bands were significantly weaker or had completely disappeared. Dotted lines indicate the regions where peak matching and band assignments were performed. In-depth analysis revealed that the 1366 cm^{-1} band showed great similarity with IMI and ACE and was associated with the C–N stretching vibration in the heterocyclic ring [20] (Fig. 6b). Investigation of the 1458-1512 cm^{-1} band showed that it matched the characteristic peaks of PYM, and these bands corresponded to the CH3 deformation vibration mode and the υ(C═C) mode of PYM, respectively [20,37] (Fig. 6c and e). Fig. 6d includes a detailed examination of the 1479 cm^{-1} band. This detected band matches the characteristic peak of IMI and reflects the δ(C–H) mode [20]. The increase in the 1582 cm^{-1} band region overlapped with the υ(C═C) vibrations of PYM + ACE [20,37] (Fig. 6f). The signal intensity in these regions is observed only in sample M7, consistent with the confirmed pesticide contamination, as determined by LC–MS/GC–MS analyses (Table S3). The weakness or absence of similar bands in clean samples (M2, M4) demonstrates that, despite the strong spectral background of the bowtie nanoarray, chemical traces of

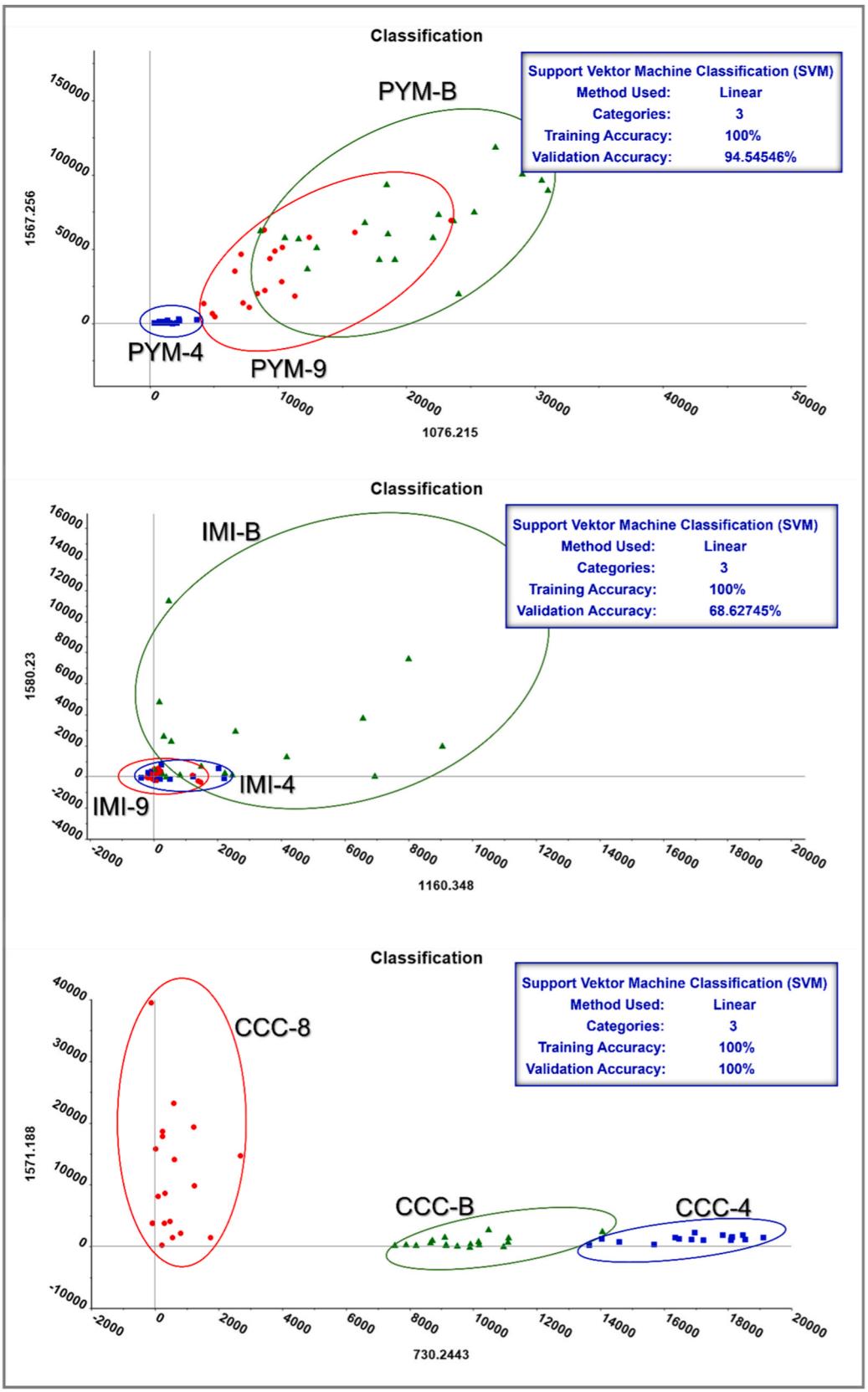

Fig. 5. Results of supervised machine learning analysis of SERS spectra of pepper waters treated with pesticides, performed using PCA-based SVM. Classification models were trained using PCA results to create training datasets; independent test samples were included for validation. Clear class separation, class boundaries, and confidence ellipses are clearly observed for the PYM, IMI, and CCC groups. The discriminative spectral features used in classification indicate that the dominant loadings obtained from PCA analyses coincide with the characteristic Raman bands of the target pesticides. Training and validation accuracy are presented in each panel.

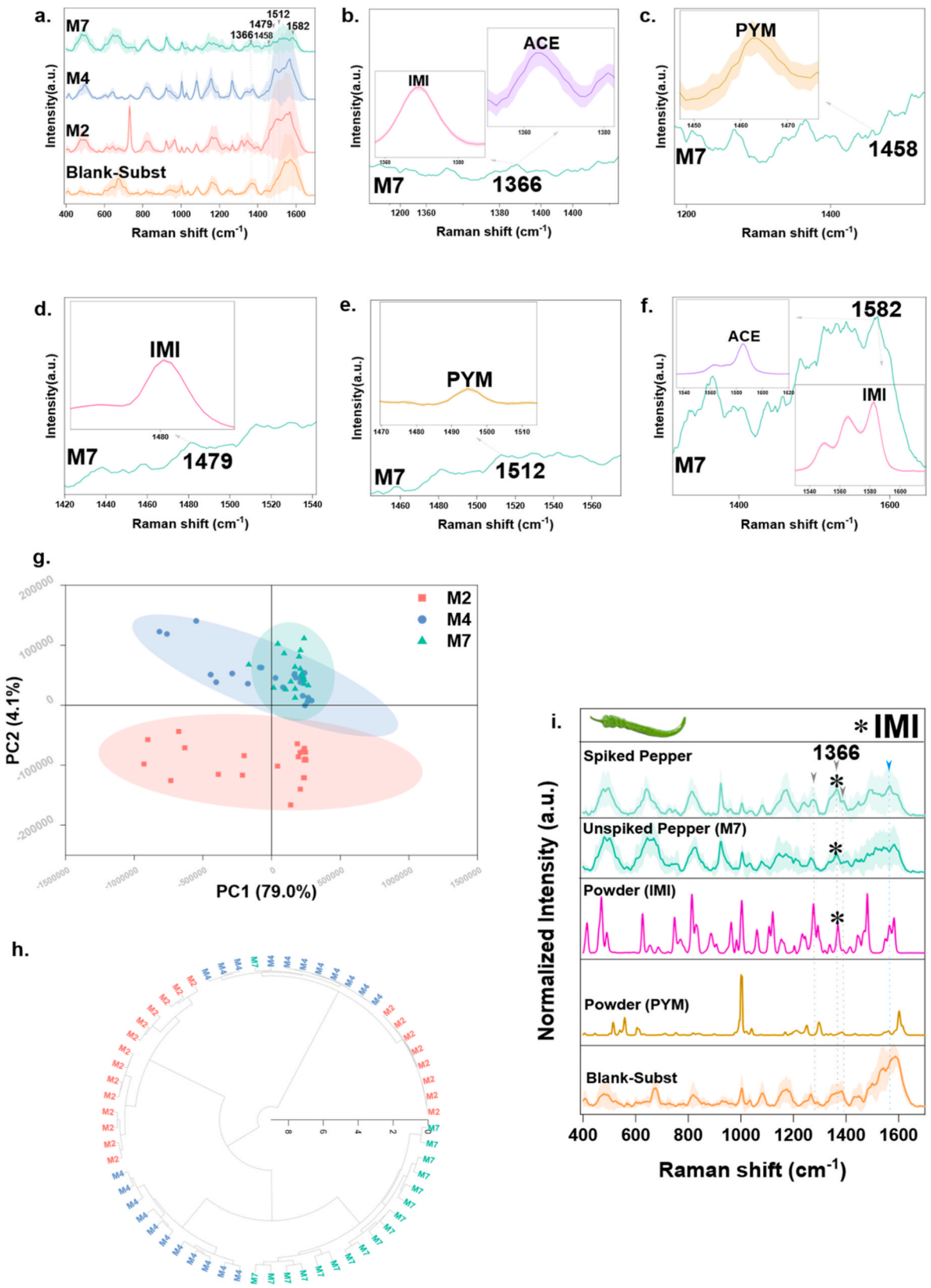

Fig. 6. SERS analysis for detection and confirmation of pesticides in real pepper samples. **a.** SERS spectra obtained from the blank (substrate), M2: Sakarya, M4: Elmalı, and M7: Mersin samples. The characteristic bands detected are shown with dotted lines. **b.** Zoomed-in view of the 1366 cm^{-1} band showing its similarity to the standard spectra of IMI and ACE. **c.** Zoomed-in view of the 1458 cm^{-1} band showing its spectral similarity to PYM. **d.** Zoomed-in view of the region where the 1479 cm^{-1} band matches IMI. **e.** Detailed view of the 1518 cm^{-1} band showing its similarity to PYM. **f.** Zoomed-in view of the 1582 cm^{-1} band showing characteristic vibrations of both PYM and ACE pesticides. **g.** PCA results for samples M2, M4, and M7 reveal clustering patterns reflecting chemical differences among the samples. HCA dendrogram of the same data set, demonstrating the level of similarity/discrimination between samples containing and not containing pesticides. **i.** Comparison of SERS spectral profiles of pesticides detected in real pepper samples with those of simulated pesticide mixtures.

pesticides can be selectively distinguished. To investigate the origin of the variation observed, SERS spectra of pepper samples collected from different regions were analyzed using PCA (Fig. 6g). The relatively high overall variation of 83.1% obtained from the analysis indicates that the data possesses strong discriminatory capacity. In this context, sample M2 (naturally grown pepper) is completely separated from the other samples and clustered in a distinct area. This separation is an expected consequence of the chemical fingerprint of samples not treated with pesticides, reflecting their natural growth conditions. The other samples are clustered together, being homogeneous within themselves and close to each other. In the HCA analysis supporting the PCA findings, the similarity and distance relationships among the samples were presented as a circular dendrogram (Fig. 6h). According to the HCA results, sample M7 is clearly distinct from the others and is in a different region. On the other hand, samples M2 and M4 appear to be in the same group and partially intermingled. This similarity is quite consistent because none of the samples contain pesticides, so their spectral fingerprints are largely limited to matrix-derived components.

To further verify the reliability of the SERS-based detection approach under real matrix conditions, clean pepper juice was simulated by adding amounts equivalent to the pesticide concentrations determined by LC–MS analysis (Table S3). The presence of the characteristic SERS band at 1366 cm^{-1} for both pesticides in both the spiked samples and naturally contaminated pepper juice confirmed the accuracy and applicability of the method (Fig. 6i) This consistency demonstrates that the SERS platform can effectively detect the same analytes in both simulated and naturally contaminated samples. Furthermore, the characteristic bands in the 1279–1390 cm^{-1} range specific to IMI, along with additional bands around 1568 cm^{-1} for both pesticides (IMI and PYM), were clearly detected, demonstrating that the analyte has multiple interaction sites with the plasmonic surface and that matrix components are measurably reflected in the overall spectral profile.

The results obtained generally offer certain advantages over traditional methods, but they also have specific limitations. Chromatography-mass spectrometry methods provide linear detection limits that are very low; however, these systems are operationally cumbersome, complex, and quite time-consuming. As detailed in Table S16 and Fig. S6, the analyte-level comparison between the SERS platform and the reference GC/LC-MS method demonstrates a high overall agreement of 93.2% across authentic market samples. This strong concordance confirms the reliability of the proposed SERS system as an effective qualitative screening tool prior to confirmatory chromatographic analysis. Our method stands out for its ability to deliver fast results, facilitate easy sample preparation, enable non-destructive detection, and distinguish even naturally grown samples spectrally. Furthermore, the high correlation between data obtained from controlled contaminated samples and real contaminated samples confirms the method's sensitivity. Thanks to its simple, economical, and environmentally friendly structure, the developed approach is seen to have high potential for use in various application areas, particularly in food safety.

4. Conclusion

The MIM-based bowtie SERS nanoarray platform has demonstrated high analytical reliability and strong matrix compatibility in both contaminated and genuine pepper extracts. The LoD values for IMI and CCC remained above the maximum residue limits set by EFSA and EPA, whereas the calculated LoD for PYM (0.16 ppm) was well below the 2 ppm limit. This suggests that PYM's stronger π-metal interaction with the metal surface, enabled by its aromatic phenyl rings, may explain this difference. Although characteristic peaks for IMI and CCC were clearly observed at low concentrations, these pesticides did not show a fully linear response to concentration. Therefore, a logistic curve model was used instead of a linear model in the LoD calculations, thereby presenting the data without manipulation and reflecting their true behavior. Furthermore, unsupervised analyses (PCA and HCA) performed on spiked and naturally contaminated samples at varying concentrations demonstrated that the system has high discriminative power even under real-matrix conditions. The detection of the same characteristic bands in simulated contaminated samples and truly contaminated samples supported the reliability of the method. Furthermore, low RSD values and consistent peak patterns in the heatmap analysis demonstrated the reproducibility of the substrate and its stability across production batches.

However, the MIM-based bowtie SERS platform has provided high reproducibility, rapid signal acquisition, and the ability to perform analyses compatible with complex matrices in both controlled contaminated and real pepper extracts. However, the system still has some limitations; the inability to maintain homogeneity in the production process of nanoarray surfaces and the complexity of field samples are among the factors that can affect reproducibility. In the future, integrating this platform into portable Raman systems and expanding it to cover residues of different pesticide classes and mixtures will further increase the method's potential for practical application and automation. Furthermore, greater integration of artificial intelligence-based algorithms into the system could improve detection sensitivity and analysis time. Therefore, the proposed MIM-based bowtie SERS approach is expected to be a promising method for the rapid, easy, and transparent detection of pesticide residues under real field conditions.

5. Supplementary data

- Phenyl ring of the PYM molecule
- Band assignments of the pesticides
- Literature Comparison
- LC-MS Validation Results
- Signal Distribution
- Linear Discriminant Analysis (LDA)
- Soft Independent Modelling by Class Analogy (SIMCA)
- Enhancement Factor Calculation
- Substrate Comparison
- Method comparison with an accredited GC/LC-MS protocol on authentic market samples
- SERS spectra of different matrices
- Comparison with EFSA limits and LOD conversions to ppm
- Inter-run RSD Analysis

CRediT authorship contribution statement

Nazlı Öncer: Writing – review & editing, Writing – original draft, Visualization, Methodology, Investigation, Conceptualization. **Sümeyra Vural Kaymaz:** Writing – review & editing, Methodology. **Elmas Eva Öktem Olgun:** Writing – review & editing, Methodology. **Oltan Canli:** Writing – review & editing, Methodology. **Barış Güzel:** Writing – review & editing. **Süleyman Çelik:** Writing – review & editing, Methodology. **Selim Tanrıseven:** Writing – review & editing, Methodology. **Hasan Kurt:** Writing – review & editing, Visualization, Supervision, Project administration, Methodology, Investigation, Funding acquisition. **Meral Yüce:** Writing – review & editing, Supervision, Project administration, Funding acquisition.

Declaration

The authors declare that they have no known conflicts of interest.

Declaration of Generative AI and generative AI-assisted technologies use

The authors used AI-assisted tools, including Grammarly, ChatGPT, and the Microsoft Word Editor, to correct spelling and grammatical errors and enhance the overall flow and readability of the text. Generative

AI was also used to translate HPLC-MS parameters (presented in the supplementary information file) from official documents originally written in Turkish. The authors have subsequently reviewed the manuscript in its entirety and assumed full responsibility for its content.

Declaration of competing interest

The authors declare that they have no known competing financial interests or personal relationships that could have appeared to influence the work reported in this paper.

Acknowledgement

The authors acknowledge the Scientific and Technological Research Council of Türkiye (TÜBİTAK) for the financial support under the 1004 calls, Project ID 22AG002. H.K. acknowledges the EU Horizon Europe Marie Sklodowska-Curie fellowship (Ref: 101111321) and UKRI MSCA fellowship (EP/Y030273/1) for the support. The authors also acknowledge useful discussions with Fahd Khalid-Salako, Efe Enes Baştuğ, Tuğçe Akbaş, and obtaining SEM images for Beyza Nur Günaydın, respectively.

Appendix A. Supplementary data

Supplementary data to this article can be found online at https://doi.org/10.1016/j.talanta.2026.129607.

Data availability

Data will be made available on request.

References

[1] Z. Chen, X. Dong, C. Liu, S. Wang, S. Dong, Q. Huang, Rapid detection of residual chlorpyrifos and pyrimethanil on fruit surface by surface-enhanced Raman spectroscopy integrated with deep learning approach, Sci. Rep. 13 (2023) 1–11, https://doi.org/10.1038/S41598-023-45954-Y;SUBJMETA.

[2] F. Álvarez, M. Arena, D. Auteri, S.B. Leite, M. Binaglia, A.F. Castoldi, A. Chiusolo, A. Colagiorgi, M. Colas, F. Crivellente, C. De Lentdecker, I. De Magistris, M. Egsmose, G. Fait, F. Ferilli, G.G. Santonja, V. Gouliarmou, K. Halling, L. H. Nogareda, A. Ippolito, F. Istace, S. Jarrah, D. Kardassi, A. Kienzler, A. Lanzoni, R. Lava, R. Leuschner, A. Linguadoca, J. Louisse, C. Lythgo, O. Magrans, I. Mangas, G. Mavriou, A. Mioč, I. Miron, T. Molnar, L. Padovani, V. Padricello, M. Panzarea, J.M. Parra Morte, S. Rizzuto, A. Romac, A. Rortais, M. Santos, R. Serafimova, R. Sharp, C. Szentes, A. Terron, A. Theobald, M. Tiramani, G. Vianello, L. Villamar-Bouza, Peer review of the pesticide risk assessment of the active substance pyrimethanil, EFSA J. 22 (2024) e8998, https://doi.org/10.2903/J.EFSA.2024.8998.

[3] EFSA, Peer review of the pesticide risk assessment for the active substance imidacloprid in light of confirmatory data submitted, EFSA J. 14 (2016) e04607, https://doi.org/10.2903/J.EFSA.2016.4607.

[4] K. Matsuda, M. Ihara, D.B. Sattelle, Neonicotinoid insecticides: molecular targets, resistance, and toxicity, Annu. Rev. Pharmacol. Toxicol. 60 (2020) 241–255, https://doi.org/10.1146/ANNUREV-PHARMTOX-010818-021747/CITE/REFWORKS.

[5] Review of the existing maximum residue levels for chlormequat according to Article 12 of regulation, EFSA J. 14 (2016), https://doi.org/10.2903/j.efsa.2016.4422.

[6] T. Yaseen, H. Pu, D.W. Sun, Fabrication of silver-coated gold nanoparticles to simultaneously detect multi-class insecticide residues in peach with SERS technique, Talanta 196 (2019) 537–545, https://doi.org/10.1016/J.TALANTA.2018.12.030.

[7] A.M. Temkin, S. Evans, D.D. Spyropoulos, O.V. Naidenko, A pilot study of chlormequat in food and urine from adults in the United States from 2017 to 2023, J. Expo. Sci. Environ. Epidemiol. 34 (2024) 317–321, https://doi.org/10.1038/S41370-024-00643-4;KWRD.

[8] Z. Chen, X. Wang, X. Ren, W. Li, L. Chen, L. Zhao, Fate and occurrence of indoxacarb during radish cultivation for multi-risk assessment, Ecotoxicol. Environ. Saf. 259 (2023) 115065, https://doi.org/10.1016/J.ECOENV.2023.115065.

[9] T. Sakthiselvi, M. Paramasivam, D. Vasanthi, K. Bhuvaneswari, Persistence, dietary and ecological risk assessment of indoxacarb residue in/on tomato and soil using GC–MS, Food Chem. 328 (2020) 127134, https://doi.org/10.1016/J.FOODCHEM.2020.127134.

[10] L. Majed, S. Hayar, S. Dousset, B.M. Maestroni, K. El Omari, Effect of Vine leaves processing on Azoxystrobin, Fenazaquin and indoxacarb residues dissipation: processing factors and consumer safety assessment, Food Chem. 447 (2024) 139065, https://doi.org/10.1016/J.FOODCHEM.2024.139065.

[11] B. Kuswandi, C.I. Fikriyah, A.A. Gani, An optical fiber biosensor for chlorpyrifos using a single sol–gel film containing acetylcholinesterase and bromothymol blue, Talanta 74 (2008) 613–618, https://doi.org/10.1016/J.TALANTA.2007.06.042.

[12] C. Ji, X. Tang, L. Wang, Y. Han, J. Wei, L. Wu, High-performance ratiometric magnetic electrochemical sensor for acetamiprid detection using Ag@PDA@Fe3O4 nanocomposites, J. Food Compos. Anal. 137 (2025), https://doi.org/10.1016/j.jfca.2024.106914.

[13] J.A. Gabaldón, A. Maquieira, R. Puchades, Development of a simple extraction procedure for chlorpyrifos determination in food samples by immunoassay, Talanta 71 (2007) 1001–1010, https://doi.org/10.1016/J.TALANTA.2006.04.041.

[14] R. Hou, S. Pang, L. He, In situ SERS detection of multi-class insecticides on plant surfaces, Anal. Methods 7 (2015) 6325–6330, https://doi.org/10.1039/C5AY01058F.

[15] M. Yilmaz, E. Babur, M. Ozdemir, R.L. Gieseking, Y. Dede, U. Tamer, G.C. Schatz, A. Facchetti, H. Usta, G. Demirel, Nanostructured organic semiconductor films for molecular detection with surface-enhanced Raman spectroscopy, Nat. Mater. 16 (2017) 918–924, https://doi.org/10.1038/NMAT4957;TECHMETA.

[16] X. Wang, S.C. Huang, S. Hu, S. Yan, B. Ren, Fundamental understanding and applications of plasmon-enhanced Raman spectroscopy, Nat. Rev. Phys. 2 (2020) 253–271, https://doi.org/10.1038/s42254-020-0171-y.

[17] M. Van Nguyen, B.T. Huy, J. Kim, Y.I. Lee, Ultrasensitive SERS substrate with high enhancement factor: silver nanoparticles on silica nanospheres for trace detection of rhodamine B, thiabendazole, and melamine, Microchem. J. 215 (2025), https://doi.org/10.1016/j.microc.2025.114082.

[18] X. Tang, C. Ji, W. Zeng, R. Wen, L. Wu, Development of an integrated EC-SPME-SERS platform with the pAg-rGO-Au substrate for ultrasensitive detection of fenthion, ACS Sens. 10 (2025) 6206–6217, https://doi.org/10.1021/acssensors.5c01968.

[19] F. Dai, A. Horrer, P.-M. Adam, M. Fleischer, F. Dai, M. Fleischer, A. Horrer, P.-M. Adam, Accessing the hotspots of cavity plasmon modes in vertical metal–insulator–metal structures for surface enhanced raman scattering, Adv. Opt. Mater. 8 (2020) 1901734, https://doi.org/10.1002/ADOM.201901734.

[20] M. Yüce, N. Öncer, C.D. Çınar, B.N. Günaydın, Z.İ. Akçora, H. Kurt, Comprehensive raman fingerprinting and machine learning-based classification of 14 pesticides using a 785 nm custom raman instrument, Biosensors 15 (2025) 168, https://doi.org/10.3390/BIOS15030168/S1.

[21] L. Pareja, V. Cesio, H. Heinzen, A.R. Fernández-Alba, Evaluation of various QuEChERS based methods for the analysis of herbicides and other commonly used pesticides in polished rice by LC–MS/MS, Talanta 83 (2011) 1613–1622, https://doi.org/10.1016/J.TALANTA.2010.11.052.

[22] D. Georgiev, S.V. Pedersen, R. Xie, Á. Fernández-Galiana, M.M. Stevens, M. Barahona, RamanSPy: an open-source python package for integrative raman spectroscopy data analysis, Anal. Chem. 96 (2024) 8492–8500, https://doi.org/10.1021/ACS.ANALCHEM.4C00383.

[23] EPA, eCFR, 40 CFR part 180 – tolerances and exemptions for pesticide chemical residues in food. https://www.ecfr.gov/current/title-40/chapter-I/subchapter-E/part-180, 2025. (Accessed 14 October 2025).

[24] H. Kurt, C. Soylukan, S. Çelik, E. Çapkın, I.C. Acuner, A.E. Topkaya, M. Yüce, Rapid and sensitive biosensing of uropathogenic E. coli using plasmonic nanohole arrays on MIM: bridging the gap between lab and clinical diagnostics, Biosens. Bioelectron. 280 (2025) 117419, https://doi.org/10.1016/J.BIOS.2025.117419.

[25] EFSA, EU pesticides database - food safety - European commission. https://food.ec.europa.eu/plants/pesticides/eu-pesticides-database_en, 2024. (Accessed 14 October 2025).

[26] TGK, Gümrük, Türk gıda kodeksi pestisitlerin maksimum Kalıntı Limitleri Yönetmeliği. https://www.gumruk.com.tr/files/turk_gida_kodeksi_pestisitlerin_maksimum_kalinti_limitleri_yonetmeligi.htm, 2025. (Accessed 30 September 2025).

[27] S. Schlücker, Surface-enhanced raman spectroscopy: concepts and chemical applications, Angew. Chem. Int. Ed. 53 (2014) 4756–4795, https://doi.org/10.1002/ANIE.201205748.

[28] J. Kneipp, K. Kneipp, Surface enhanced nonlinear raman processes for advanced vibrational probing, ACS Nano 18 (2024) 20851–20860, https://doi.org/10.1021/ACSNANO.4C07508.

[29] C. Zong, M. Xu, L.J. Xu, T. Wei, X. Ma, X.S. Zheng, R. Hu, B. Ren, Surface-enhanced raman spectroscopy for bioanalysis: reliability and challenges, Chem. Rev. 118 (2018) 4946–4980, https://doi.org/10.1021/ACS.CHEMREV.7B00668.

[30] V. Smeliková, I. Kopal, M. Člupek, M. Dendisová, M. Švecová, Unveiling the crucial role of chemical enhancement in the SERS analysis of amphetamine–metal interactions on gold and silver surfaces: importance of selective amplification of the narrow interval of vibrational modes, Anal. Chem. 96 (2024) 5416–5427, https://doi.org/10.1021/ACS.ANALCHEM.3C05189.

[31] P. Wang, L. Wu, Z. Lu, Q. Li, W. Yin, F. Ding, H. Han, Gecko-inspired nanotentacle surface-enhanced raman spectroscopy substrate for sampling and reliable detection of pesticide residues in fruits and vegetables, Anal. Chem. 89 (2017) 2424–2431, https://doi.org/10.1021/ACS.ANALCHEM.6B04324.

[32] B. Hu, D.W. Sun, H. Pu, Q. Wei, Rapid nondestructive detection of mixed pesticides residues on fruit surface using SERS combined with self-modeling mixture analysis method, Talanta 217 (2020) 120998, https://doi.org/10.1016/J.TALANTA.2020.120998.

[33] C. Li, Z. Chen, Y. Huang, Y. Zhang, X. Li, Z. Ye, X. Xu, S.E.J. Bell, Y. Xu, Uncovering strong π-metal interactions on Ag and Au nanosurfaces under ambient conditions via in-situ surface-enhanced Raman spectroscopy, Chem 8 (2022) 2514–2528, https://doi.org/10.1016/J.CHEMPR.2022.06.008.

[34] Y. Xu, Y. Zhang, C. Li, Z. Ye, S.E.J. Bell, SERS as a probe of surface chemistry enabled by surface-accessible plasmonic nanomaterials, Acc. Chem. Res. 56 (2023) 2072–2083, https://doi.org/10.1021/ACS.ACCOUNTS.3C00207.
[35] T. Zhang, R. Lu, G. Wang, X. Sun, J. Li, B. Mizaikoff, Glucose sandwich assay based on surface-enhanced Raman spectroscopy, Analyst 148 (2023) 4310–4317, https://doi.org/10.1039/D3AN00481C.
[36] U.T. Uthappa, M. Nehra, R. Kumar, N. Dilbaghi, G. Marrazza, A. Kaushik, S. Kumar, Trends and prospects of 2-D tungsten disulphide (WS2) hybrid nanosystems for environmental and biomedical applications, Adv. Colloid Interface Sci. 322 (2023) 103024, https://doi.org/10.1016/J.CIS.2023.103024.
[37] Daimay Lin-Vien, N.B. Colthup, W.G. Fateley, J.G. Grasselli, The Handbook of Infrared and Raman Characteristic Frequencies of Organic Molecules, Academic Press, 1991.